# Engineered extracellular vesicle-delivered TGF-β inhibitor for attenuating osteoarthritis by targeting subchondral bone

**Zhaopu Jing**(iD)**, Guangyang Zhang, Yuanqing Cai, Jialin Liang, Leifeng Lv and Xiaoqian Dang**(iD)

## Abstract

Osteoarthritis (OA) is a disease that affects the entire joint. To treat OA, it may be beneficial to inhibit the activity of TGF-β in the subchondral bone. However, delivering drugs to the subchondral bone using conventional methods is challenging. In this study, we developed an extracellular vesicle delivery system. The utilization of macrophage-derived extracellular vesicles as a drug-carrying platform enables drugs to evade immune clearance and cross biological barriers. By incorporating targeting peptides on the surface of extracellular vesicles, the drug platform becomes targeted. The combination of these two factors results in the successful delivery of the drug to the subchondral bone. The study evaluated the stability, cytotoxicity, and bone targeting capability of the engineered extracellular vesicle platform (BT-EV-G). It also assessed the effects of BT-EV-G on the differentiation, proliferation, and migration of bone mesenchymal stem cells (BMSCs). Additionally, the researchers administered BT-EV-G to anterior cruciate ligament transection (ACLT)-induced OA mice. The results showed that BT-EV-G had low toxicity and high bone targeting ability both in vitro and in vivo. BT-EV-G can restore coupled bone remodeling in subchondral bone by inhibiting pSmad2/3-dependent TGF-β signaling. This work provides new insights into the treatment of OA.

## Keywords

Osteoarthritis, extracellular vesicles, bone targeting peptide, TGF-β, subchondral bone

The Second Affiliated Hospital of Xi'an Jiaotong University, Xi'an, China
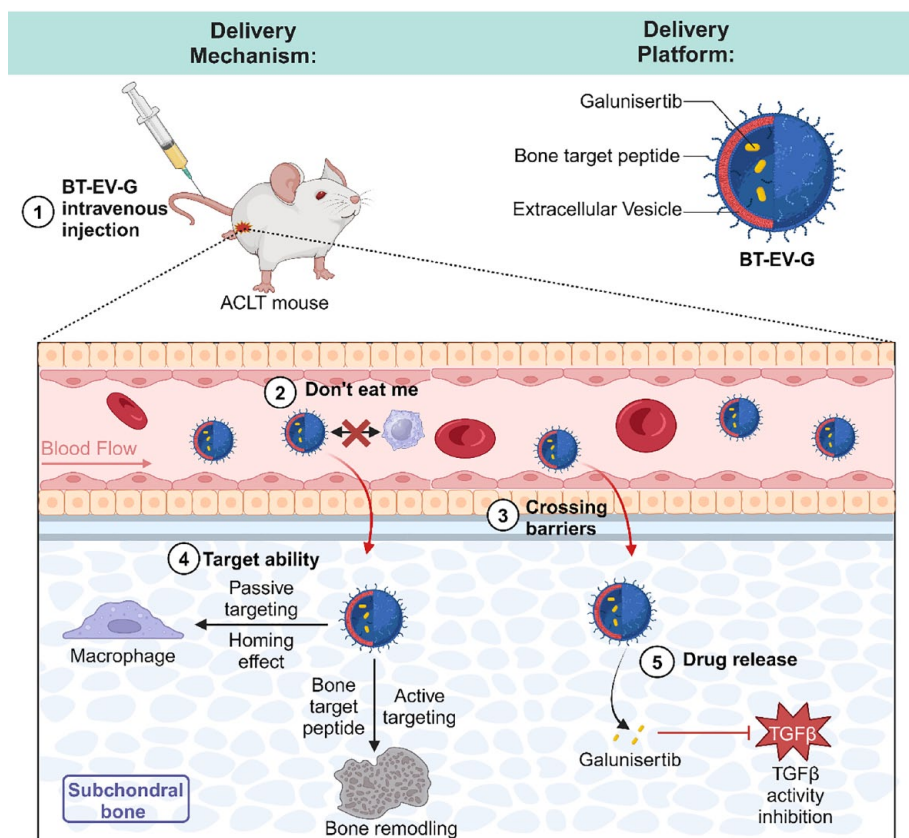
**Corresponding author:**
Xiaoqian Dang, The Second Affiliated Hospital of Xi'an Jiaotong University, No. 157, Xiwu Road, Xi'an 710004, China.
Email: dangxiaoqian@xjtu.edu.cn

**Graphical Abstract**

Mechanism of Engineered Extracellular Vesicle-Delivered TGF-β Inhibitor for Attenuating Osteoarthritis by Targeting Subchondral Bone.



## Introduction

Osteoarthritis (OA) is the most prevalent joint disease globally,[1] affecting an estimated 10% of men and 18% of women over the age of 60, with a total of 250 million people currently affected worldwide.[2] The resulting socio-economic burden is considerable, amounting to between 1% and 2.5% of gross domestic product in developed countries.[3] Despite the significant public health burden and increasing prevalence of OA, current treatment options focus on symptomatic improvement and include paracetamol, NSAIDs, opioids, analgesics, and intra-articular medications (e.g., steroids and hyaluronic acid). These treatments are largely palliative in nature.[4] Surgery is usually only indicated as a treatment of last resort for patients with end-stage OA.[5] Despite the significant impact and disease burden on OA patients, no drugs have been approved by regulatory agencies as effective disease-modifying osteoarthritis drugs (DMOADs).[6] Consequently, there is a significant unmet need for current treatments. The discovery of innovative, effective DMOADs is crucial to reducing the disease burden.

Due to the substantial inter-patient variability in clinical manifestations and pathologic changes observed in OA, identifying patient/disease subtypes suitable for targeted therapy may represent a promising avenue for future drug development research.[7,8] In general, OA can be categorized into three subtypes based on the main drivers of the disease: (1) synovitis-driven subtypes, (2) cartilage-driven subtypes, and (3) bone-driven subtypes.[9] In recent years, the role of subchondral bone in the progression of OA has gradually attracted the attention of researchers due to the unsatisfactory results of treatments targeting the articular cartilage or synovial components. In early OA, overactivated bone remodeling is prevalent at sites of microinjury in the subchondral bone. This results in the over-activation of TGF-β in the microenvironment of the subchondral bone, which in turn leads to the recruitment of bone progenitor cells to the site of bone remodeling through the activation of the Smad2/3 pathway. This promotes the osteogenic differentiation of bone progenitor cells, ultimately resulting in the formation of osteoid islet. The formation of osteoid islet, in turn, exacerbates the abnormal mechanical stress and accelerates the deterioration of

OA.[10] Consequently, the inhibition of the TGF-β signaling pathway in the subchondral bone may represent a promising avenue for future research.

However, targeting the subchondral bone for drug delivery presents numerous challenges. First, cartilage itself is a dense biological barrier, rendering it difficult for drugs to cross the cartilage layer and reach the subchondral bone through intra-articular injection.[11] Second, systemic drug delivery can result in biological clearance of the majority of the drug, making it challenging to create an effective drug concentration at the localized lesion.[12] Nanomedicine may offer a potential solution to these issues. Nanomedicine represents an innovative aspect of nanotechnology that aims to enhance healthcare by integrating chemical, physical, and biological sciences to develop multidisciplinary diagnostic and therapeutic approaches at the nanoscale.[13] An important aspect of nanomedicine is the use of nanocarriers for therapeutic purposes, with the objective of overcoming the shortcomings of conventional drugs. The in vivo clearance and tissue distribution of therapeutic drugs are largely determined by the characteristics of the carrier rather than the physicochemical properties of the drug molecule when carried by drug delivery systems.[14]

Extracellular vesicles represent a prominent example of nano drug delivery systems.[15] One of the principal reasons why extracellular vesicles are favored as drug delivery systems is their excellent biocompatibility. While conventional drug delivery systems (e.g., liposomes, nanoparticles, polymers) frequently encounter immune recognition and clearance problems in vivo, extracellular vesicles, due to their biological origin, are likely to be less reactive to the immune system, which helps to minimize the toxic effects of the foreign substance once it enters the body.[16] There is evidence that EVs have satisfactory performance in plasma stabilization.[17] During transfusion, a significant amount of EVs of hematopoietic origin in the blood is transferred to the patient, yet it does not cause significant adverse effects.[18] In a clinical trial, intrathoracic injection of tumor cell-derived EVs loaded with chemotherapeutic agents resulted in only low-grade toxicity while yielding clinical benefits.[19] Furthermore, EVs do not appear to cause toxicity or inflammatory responses even after external modification. For instance, studies modifying C2C12 cell-derived EVs with anchor peptides and splice-converting oligonucleotides for the treatment of muscular dystrophy demonstrated that no toxicity or inflammatory response was detected in the liver, kidney, or muscle of mice after intravenous injection of EVs.[20] These results suggest that EVs have good immune tolerance, even when used heterologously. It is well known that one of the major difficulties faced by conventional drug delivery systems is the inability to effectively cross biological barriers. In contrast, several studies have demonstrated that EVs can effectively cross these biological barriers and induce functional changes in target cells. At the tissue level, EVs have been shown to cross the blood-brain barrier.[21] The blood-brain barrier is one of the most challenging barriers to drug delivery systems, and EVs are able to cross the blood-brain barrier through the choroid plexus to reach the brain parenchyma, with the ability to transport therapeutic cargo across the blood-brain barrier.[22] At the cellular level, EVs are capable of interacting with the plasma membrane and entering the interior of the cell, rather than aggregating at the cell surface.[23,24] Furthermore, extracellular vesicles may be more efficiently internalized by cells than other drug carriers.[25]

Nevertheless, the clinical application of natural EVs as drug delivery systems remains constrained. This is due to the fact that EVs are prone to being trapped in non-specific tissues, particularly in the liver and lungs, which results in inadequate targeting in vivo.[26] Furthermore, they are rapidly cleared by the reticuloendothelial system after systemic administration, thus limiting the dose of drug reaching the target organ.[27] There is mounting evidence that the engineering of EVs can enhance their targeting ability and therapeutic efficacy.[28] Additionally, there is growing interest in modifying EV membranes to target specific tissues for the purpose of improving or enhancing therapeutic efficacy.[29] For instance, Jia et al.[30] constructed NPR-1-modified macrophage-derived EVs that successfully crossed the blood-brain barrier and delivered curcumin to gliomas, thereby providing a potential approach for intracranial tumor treatment. Wang et al.[31] used aptamer AS1411-modified EVs have been employed to deliver siRNA/microRNA for targeted delivery to breast cancer tissues. Lin et al.[32] modified peptide cNGQGEQc to the surface of EVs for non-small cell lung cancer targeting. Liang et al. fused peptide CAP to EV surface-associated proteins to obtain chondrocyte-targeted EVs, which inhibited the progression of OA in rats.[33]

Therefore, we constructed macrophage-derived extracellular vesicles with the peptides DSS[6] and encapsulated Galunisertib. Macrophage-derived EVs have two advantages. First, macrophages are enriched for inflammation at osteoarthritis joints,[34] and the homing effect makes them naturally joint-targeted,[35] which facilitates the accumulation of therapeutic cargo at localized lesions after systemic injection. Second, macrophage-derived EVs express CD47 on the surface, which is a "don't eat me" signal that can evade clearance by the reticuloendothelial system, which helps to thereby reduce the dose of the drug used and minimize off-target effects.[36] In addition, we further enhanced the targeting properties of EVs by loading designed targeting ligands onto the surface of EVs. In comparison to other bone-targeting materials (e.g., bisphosphonates, tetracyclines), oligopeptides containing repeating Asp or Glu units exhibit several advantages, including high stability, good tissue permeability, low immunogenicity, and the capacity to be metabolized into nontoxic substances.[37] Of

particular note is the ability of DSS[6] to be further targeted to the site of bone remodeling, which is highly compatible with our anticipated therapeutic targets.[38] Consequently, DSS[6] is an optimal ligand for bone targeting. Among the TGF-β inhibitors, we selected Galunisertib. Galunisertib is a small molecule compound with hydrophobicity. Due to its hydrophobicity, it can be loaded into EVs through simple incubation. Compared to loading methods such as sonication and electrotransfer, simple incubation is the least damaging to EVs and the simplest for mass production.[39] A comprehensive study was conducted to assess the physicochemical properties and biocompatibility of BT-EV-G, ensuring its suitability for use in OA. In vivo and in vitro assays were performed to verify the targeting of DSS[6]-modified EVs. To gain insight into the far-reaching effects of BT-EV-G in vivo and in vitro, several comprehensive evaluations were conducted, including histologic, imaging, and functional studies. It is of significant importance to note that the phenotypes of BMSCs migration, proliferation, and differentiation were tested in order to elucidate the detailed mechanisms by which BT-EV-G inhibits abnormal ossification in the subchondral bone microenvironment. Overall, BT-EV-G targeted OA subchondral bone and inhibited OA progression. This finding has important clinical therapeutic implications for OA and other related orthopedic diseases.

## Materials and methods

### Animal studies

Male BALB/c mice were obtained from the Experimental Animal Centre of Xi'an Jiaotong University, China. The mice were kept in specific pathogen-free (SPF) rooms at the animal center. All animal care protocols and experiments in this study followed the approved protocols of the animal center. Five groups of male BALB/c mice, aged 12 weeks, were randomly assigned (*n*=5 per group) as follows: sham, anterior cruciate ligament transverse (ACLT) alone, and ACLT followed by treatment with G, EVs and BT-EV-G. Each treatment group received once every 3 days intravenous injection of PBS (100 μL) containing $1.0 \times 10^{11}$ particles per mL through the tail vein for 30 days. The sham and ACLT alone groups received once every 3 days intravenous injection of PBS (100 μL) for 30 days. Throughout the experiment, animals had unrestricted access to food and water. The mice were euthanized by inhaling Isoflurane.

### Cell culture

Primary BMSCs were isolated and cultured from newborn BALB/c mice (1–3 days old) in Dulbecco's Modified Eagle Medium (DMEM) supplemented with 10% FBS, penicillin (100 IU mL$^{-1}$), and streptomycin (100 μg mL$^{-1}$).

The Raw 264.7 cell line was commercially obtained from Procell Life Science & Technology (Wuhan, China). Raw264.7 cells were cultured in Dulbecco's Modified Eagle Medium (DMEM) supplemented with 10% fetal bovine serum (FBS), 1 penicillin (100 IU mL$^{-1}$), and streptomycin (100 μg mL$^{-1}$). The cells were maintained at 37°C with 5% $CO_2$ and the medium was replaced every 3 days. When the cells reached 70%–80% confluence, they were reseeded into a suitable culture dish. Only BMSCs with passage numbers below 10 were used in this study.

### Extracellular vesicle isolation and characterization

Raw264.7 cells were cultured in serum-free DMEM medium for 48 h. The conditioned medium was then harvested and centrifuged at 300 g for 10 min to remove dead cells, followed by centrifugation at 2000 g for 10 min to remove cell debris. The supernatant was transferred to a 0.22 μm cell filter (Merck KGaA, Darmstadt, Germany) to remove large vesicles. Finally, the filtrate was concentrated using a 100kd ultrafiltration tube (Merck KGaA, Darmstadt, Germany) at 4000 g for 30 min. All steps were carried out at 4°C.[40] The total protein concentration of the extracellular vesicle suspension was measured using a BCA protein assay kit (Beyotime Institute of Biotechnology, Shanghai, China).[41] The diameters and zeta potentials of the extracellular vesicle were analyzed by dynamic light scattering (DLS) using Litesizer 500 (Anton Paar, Shanghai, China).[42] The same method was used to measure the physiological stability of extracellular vesicles. The same sample was tested for diameters and zeta potentials for seven consecutive days. The morphology was observed under a TEM (Talos L 120C G2, Thermo Fisher Scientific Inc) at a 100 keV accelerating voltage. TEM samples were prepared by negative staining with uranyl acetate.

### Modification of extracellular vesicle with bone-targeting peptide

The bone-targeting peptide (DSPE-PEG-Mal-Cys-DSS[6], 90.64% purity as determined by HPLC) was synthesized by ChinaPeptides (Shanghai, China). To combine the extracellular vesicle with the bone-targeting peptide, 10 μL of extracellular vesicle (2 mg/mL) and 90 μL of DSPE-PEG-Mal-Cys-DSS[6] (10 μM) were gently added to PBS (100 μL). The mixture was then incubated overnight at 4°C. To remove any uncombined DSPE-PEG-Mal-Cys-DSS,[6] the mixture was extracted using the extracellular vesicle isolation method. To confirm successful modification of the extracellular vesicle, we combined the peptide labeled with fluorescein isothiocyanate (FITC) and

observed the fluorescence signal using a fluorescence microscope (NovoCyte, ACEA Biosciences, USA).[43] Concentration ratio of EV:FITC = 1 mg:150 µg.

## Loading of Galunisertib into BT-EV

BT-EV (3 mg) and Galunisertib (3 mg, Topscience Co. Ltd) were dissolved in PBS (3 mL) and deionized water (6 mL) was added using a peristaltic pump under continuous stirring overnight. The mixture was dialyzed against deionized water for 3 h, with the dialysate being changed every half an hour. The amount of Galunisertib loaded in the Extracellular vesicles was determined via HPLC by comparing the absorbance of the BT-EV-Galunisertib dispersions at 254 nm with the Galunisertib standard concentration curve.[44]

## Cytotoxicity assays in vitro

Cell viability was evaluated using the CCK-8 assay. The cells (MC3T3-E1, 96-well plate inoculation, 10,000 cells per well) were treated with EVs and BT-EV-G at varying concentrations and incubated for 24 h. The CCK-8 kit was used to examine cell viability following the established protocols.[45]

## Cellular uptake of EVs in vitro

Cellular uptake was evaluated using fluorescence microscopy. BMSCs were seeded into observation dishes at a density of $1 \times 10^4$ cells per dish for fluorescence microscopy. Once the cells reached 80% confluence, the medium was replaced with DMEM containing EVs or BT-EV-G labeled with PKH26 and incubated at 37℃. After 4 h of treatment, the supernatant was carefully removed, and the cells were gently washed three times with PBS before being fixed with 4% paraformaldehyde for 15 min. The cells were washed three more times and then stained with Phalloidin for 30 min. After that, the cells were washed three more times and stained with 4′,6-diamidino-2-phenylindole (DAPI) for 5 min. Finally, the cells were observed under fluorescence microscopy (Axiocam 305 color, Carl Zeiss AG, Germany).[46]

## PKH26 marked EVs

Mix 500 µL of EVs at a concentration of 1 mg/mL with 1 mL of "Diluent C." Dilute 4 µL of "PKH26 stock solution" with 1 mL of "Diluent C" to prepare a 4 µM working solution of the dye. Mix the liquids of the above two steps quickly and incubate for 5 min away from light. Extract the EVs again by the same way as for EVs in order to remove excess dye. PKH26 kit was purchased from Shanghai Maokang Biotechnology Co., Ltd.

## HA binding tests

The EVs and BT-EVs were first labeled with the PKH26 fluorescent probe. The PKH26-labeled extracellular vesicles were then diluted to a concentration of 0.8 mg mL$^{-1}$, and the initial fluorescent intensity was measured using fluorescence spectroscopy (λex = 551 nm, λem = 567 nm). Next, HA (25 mg, Nanjing Duly Biotech Co., Ltd.) was added to the PKH26-labeled EVs and PKH26-labeled BT-EVs (4 mL). Binding experiments were conducted at 37℃ with continuous stirring at 100 rpm for 3 h. The suspension was then centrifuged, and the fluorescent intensity of the supernatant was measured.[47]

## Tissue-specific delivery in vivo

DSS[6] was labeled with FITC. To label bone formation surfaces, Xylenol Orange (XO) was injected intra-abdominally in mice 3 days prior to the administration of FITC or DSS[6]-FITC.[38,48] These fluorescent compounds were administered to the mice via tail vein injection at a dose of 27 µmol kg$^{-1}$ in 200 µL PBS, respectively, following anesthesia with Isoflurane. The mice were sacrificed 24 h after administration for processing of undecalcified tissue sections. The tibia was dehydrated using graded concentrations of ethanol and embedded in modified methyl methacrylate without decalcification. Frontal sections of the proximal tibia were obtained at a thickness of 10 µm using HistoCore AUTOCUT (Leica, Germany). The fluorescence intensity of FITC was visualized using BX53 (Olympus, Japan).

## Organ-specific delivery in vivo

Six mice were divided into two groups and exposed to Cy5.5 labeled G at a dose of 0.3 mg/mL and 0.2 mL or Cy5.5 labeled BT-EV-G at a dose of 1 mg/mL and 0.2 mL via tail vein injection. Four hours later, the mice were sacrificed and the major organs (brain, heart, liver, spleen, lung, kidney, femur, and tibia) were collected. Imaging was performed using a small animal in vivo imaging system VISQUE in vivo smart-LF (Vieworks, Korea).[49]

## Cell proliferation assay

EdU-555 Cell Proliferation Assay Kit (Beyotime, Shanghai, China) was used to evaluate the proliferation of BMSCs stimulated with different treatment.

BMSCs were inoculated in 96-well plates at a density of 10,000 per well. The experiment was divided into five groups, PBS group, TGF-β group (TGF-β 10 ng/mL), TGF-β + G group(TGF-β 10 ng/mL, G 10 ng/mL), TGF-β + EVs group(TGF-β 10 ng/mL, EVs 250 µg/mL), TGF-β + BT-EV-G group (TGF-β 10 ng/mL, BT-EV-G 250 µg/mL). After 24 h of different treatments, an equal volume of

"EdU working solution" was added to each well. Incubation was continued in the cell incubator for 2 h. The cells were then fixed with 4% paraformaldehyde for 15 min and were permeabilized with 0.3% TritonX-100 for 15 min. Prepare "Click Reaction Solution" according to the method provided in the kit. "Click Reaction Solution"(0.5 mL) was added to each well and incubated for 30 min at room temperature in the dark. Then "Hoechst"(1 mL) was added to each well and incubated for 10 min at room temperature in the dark. After washing with PBS, images were captured under a fluorescence microscope. Azide 555 $\lambda_{ex}=555$ nm, $\lambda_{em}=565$ nm; Hoechst $\lambda_{ex}=346$ nm, $\lambda_{ex}=460$ nm.[28]

## Cell migration assay

The migration of BMSCs treated with different groups was evaluated by a transwell migration assay based on a transwell chamber, as described in the previous research.[50] BMSCs were inoculated in 24-well plates at a density of 5000 per well. The experiment was divided into five groups, as described in "Cell Proliferation Assay." Briefly, 600 µL of complete medium, TGF-β and different types of exosomes were added to the lower chamber of the transwell chamber system, and 200 µL of medium containing cells was added to the upper chamber of the transwell chamber system (3421; Corning, USA). The cells were then allowed to migrate to the bottom surface of the chambers for 24 h. After cell migration, a clean cotton swab was used to carefully and completely remove the unmigrated cells in the upper chamber, and the migrated cells on the bottom surface were fixed in 4% paraformaldehyde. After fixation with paraformaldehyde, the cells were stained with 0.2% crystal violet. After air drying the chamber at room temperature, the crystal violet-stained cells were observed under a microscope as they migrated through the membrane pores and reached the bottom of the chambers. Quantitative analysis of cell migration was performed using ImageJ software at the endpoint.

## Cell differentiation assay

Differentiation of Extracellular vesicles-stimulated cells was determined by alkaline phosphatase (ALP) and alizarin red S (ARS) staining, which were performed as previously described.[51] BMSCs ($1 \times 10^5$ cells per well) were seeded separately in 24-well plates. After seeding, the cells were cultured overnight at 37°C to allow for complete adhesion. After cell attachment, the medium was replaced with DMEM supplemented with osteogenic induction factors (10 nM dexamethasone, 5 mM β-glycerophosphate, and 50 µg mL$^{-1}$ ascorbic acid). For all cultures, the medium was changed every 3 days. For ALP staining, cells were treated for 7 days. Briefly, the cells were gently washed three times with PBS, fixed in 4% paraformaldehyde for 15 min, and then evaluated with an ALP assay kit

(Beyotime, Shanghai, China) according to the manufacturer's protocol. Each plate was observed and photographed under an inverted microscope. ImageJ software was used for semiquantitative analysis. For ARS, cells were treated for 21 days. After washing and fixing as above, the cells were stained with 2% Alizarin Red S (Beyotime, Shanghai, China) for 15 min and gently washed with PBS. After photographing, the alizarin red was extracted with 10% cetylpyridinium chloride, and then the absorbance was measured at 562nm to compare the alizarin red content.

## qRT-PCR

Cells were harvested and treated with Trizol reagent to obtain total RNA following the supplier's protocols. The concentration of RNA was determined using a DS-11 spectrophotometer (DeNovix, USA). Next, miRNA samples were reverse transcribed using a HisScript II Q RT SuperMix for qPCR kit (Vazyme, Nanjing, China). qRT-PCR was conducted in triplicate using a qPCR SYBR Green Master Mix kit (Yeasen, Shanghai, China). The relative expression difference was determined using the comparative Ct (2-ΔΔCt) method.[52]

The following primers were used: GAPDH: forward 5′-GGA AGCTTGTCATCAAT GGAAATC-3′ and reverse 5′-TGATGACCCTTTTGGCTCCC-3′; ALP: forward 5′-CTCCTCGGAAGACACTCTGACC-3′ and reverse 5′-CT GCGCCTGGTAGTTGT TGTG-3′; RUNX2: forward 5′-CTACTATGGCACTTCGTCAGGAT-3′ and reverse 5′-ATCAGCGTCAACACCATCATT-3′; OCN: forward 5′-CCTCACACTCCTCGC CCTATT-3′ and reverse 5′-CCG ATGTGGTCAGCCAACTC-3′; OPN: forward 5′-C AGT GATTTGCTTTTGCCTCC-3′ and reverse 5′-ATCT GGGTATTTGTTGTAA AG CTGC-3′; Osterix: forward 5′-TTTACCCGAAGCGACCACC-3′ and reverse 5′- G AGTGATTGGCAAGCAGTGGTC-3′.

## Western blot analysis

The EVs were not lysed and were directly mixed with Loading Buffer and denatured at high temperature. Cell-derived proteins were performed by isolating total proteins from harvested cells using a protein extraction kit (Beyotime, Shanghai, China) following the manufacturer's protocols. Equal amounts of protein samples(5 µL, 1 mg/mL) were loaded and separated by SDS-PAGE, then transferred to 0.22 µm polyvinylidene difluoride (PVDF) membranes. The membranes were blocked with 5% skimmed milk and incubated with specific antibodies overnight. The primary antibodies used were: CD9 (1:1000), CD63 (1:1000), and TSG101 (1:1000) antibodies were obtained from Abcam. The membranes were then incubated with horseradish peroxidase (HRP)-labeled secondary antibodies for 1 h at room temperature.[45]

### Immunofluorescence staining was performed on osteoblasts

The BMSCs were incubated with different Extracellular vesicles, fixed with 4% paraformaldehyde for 15 min at room temperature, and then permeabilized in 0.5% Triton X-100 for 15 min. ALP, Runx2, and OCN were stained using their respective antibodies (ALP, Runx2, OCN; Proteintech, Wuhan, China). Nonspecific binding was blocked using 1% BSA. The secondary antibodies labeled with Cyanine 3 (Cy3, Servicebio, Wuhan, China) were incubated with the primary antibodies of ALP, Runx2, and OCN. DAPI (blue) and Phalloidin (green) were used to respectively stain the nuclei and actin filaments. The cells were imaged using confocal laser scanning microscopy (CLSM). Immunofluorescence staining was quantified using ImageJ software.[53]

### Histochemistry, immunohistochemistry, and histomorphometry analysis

Tibia bone samples and organs (heart, liver, spleen, lung, and kidney) from the different groups were fixed in 4% paraformaldehyde for 48 h. Bone samples were decalcified for 2 months with 0.5M ethylene diamine tetraacetic acid (EDTA). Each organ was embedded in paraffin, sliced into 4 μm sections, and stained with hematoxylin and eosin (H&E). The bone samples were embedded in paraffin and then cut into 4 μm-thick longitudinal-oriented sections. These sections were processed for H&E and Safranin O and fast green staining. Tartrate-resistant acid phosphatase (Trap) staining was conducted using a standard protocol. Sagittal sections of the tibia were incubated with primary antibodies against nestin, osterix, pSmad2/3, MMP13, collagen II, and aggrecan (all from Servicebio, Wuhan, China) at 4℃ overnight. For immunofluorescence staining, secondary antibodies conjugated with fluorescence were incubated for 1 h at room temperature while avoiding light. Histomorphometric measurements were performed on the entire area of the tibia subchondral bone using the Panoramic histiocvte quantitative analysis system from Zeiss, Germany. The Osteoarthritis Research Society International-modified Mankin criteria (OARSI) scores were calculated as previously described.[54]

### Micro-CT analysis

The data was analyzed using VG Studio MAX data analysis software. The tibias were fixed using 4% paraformaldehyde for 48 h and scanned with an AX-2000 CT scanner (Always, Shanghai, China) at a voltage of 160 kV, current of 0.5 mA, and resolution of 2 μm per pixel. The region of interest covered the entire subchondral bone media compartment. Three-dimensional histomorphometric analysis was performed using longitudinal images of the tibial subchondral bone. The study analyzed three-dimensional structural parameters including TV (total tissue volume, which contains both trabecular and cortical bone), Tb.Pf (trabecular pattern factor), and subchondral bone plate thickness (SBP).[55]

### Statistical analysis

The numerical data is presented as the mean ± standard deviation (SD). For statistical analysis, one-way ANOVA was used for three or more groups, and Student's t-test was used for two groups, using GraphPad Prism 9.0. Homogeneity of variance was tested first and then the differences between groups were assessed by post hoc multiple comparisons. Specifically, if no heterogeneity was observed, the Bonferroni test was used to assess the differences between groups. However, if heterogeneity did exist, the Welch test was used to test the equality of means and the Dunnett's T3 was used to assess the differences between groups. The level significance was set at $p < 0.05$. NS, no significant difference; *, $p < 0.05$; **, $p < 0.01$; ***, $p < 0.001$.

## Results and discussion

### Preparation and characterization of engineered extracellular vesicles

Extracellular vesicles derived from macrophages were isolated from the supernatant of cultured Raw264.7 cells. The modification process of engineered extracellular vesicle (BT-EV-G) is shown in Figure 1(a). Transmission electron microscopy revealed that these particles have a typical cup-shaped morphology (Figure 1(b)). Dynamic light scattering and nanoparticle tracking analysis showed that the mean diameter of the extracellular vesicles was $99.9 \pm 13.9$ nm (Figure 1(d)). Western blotting confirmed the high expression of specific protein markers CD9, CD63, and TSG101 in the extracellular vesicles (Figure 1(f)). These results indicate the successful isolation of extracellular vesicles from the conditioned medium.

As the extracellular vesicle surface does not allow for direct insertion of DSS,[6] while DSPE-PEG could be inserted into the extracellular vesicle surface, we have customized the trimmed bone targeting peptide (DSPE-PEG-Mal-Cys-DSS[6]). For the bone-targeting modification of extracellular vesicle, EVs were conjugated with the DSPE-PEG-Mal-Cys-DSS[6] through a diacyllipid insertion method. To verify the successful modification of EVs, the carboxyl terminal of the peptide was labeled with a FITC fluorophore (green) and extracellular vesicles were labeled with PKH26 (red). The mixture was then incubated for 3 h at room temperature under continuous stirring (100 rpm). The extracellular vesicles were
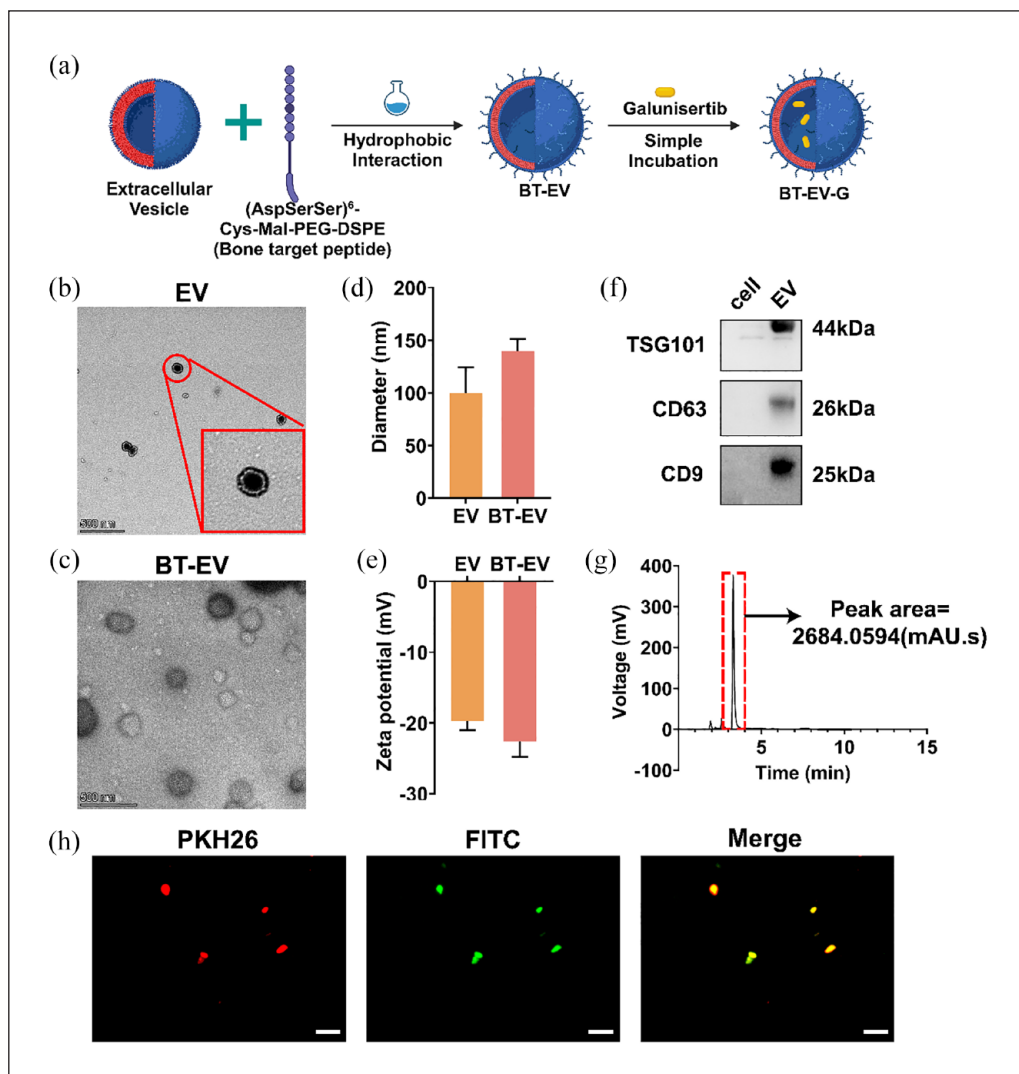
**Figure 1.** Preparation and characterization of BT-EV. (a) Schematic of modification of BT-EV-G. (b) TEM image of EV. Scale bar = 100 nm, (c)TEM image of BT-EV. Scale bar = 100 nm. (d) Size distribution of EV and BT-EV measured by DLS. (e) Zeta potential of EV and BT-EV. (f) Western blot analysis of EV-associated proteins, TSG101, CD63, CD9. (g) HPLC of drug loading into extracellular vesicles. (h) Fluorescence images of BT-EV, the red fluorescence represents PKH26-EV, the green fluorescence represents FITC-bone targeting peptide. Scale bar = 500 nm.

extracted again using the same extraction method to remove any excess uninserted peptides. The co-localization of red and green fluorescence on the EVs membrane indicated successful anchoring of the bone-targeting peptide DSS[6] onto the surface (Figure 1(h)). Subsequently, drugs (Galunisertib) were loaded into BT-EV using a simple incubation technique. The loading efficiency was measured by HPLC. The HPLC was used to measure the peak areas of various drug standards at different concentrations, establishing a standard curve between peak area and drug concentrations (Figure S1). After co-incubating the drug and EVs and removing any unloaded drug, the peak area of drug within the EVs was measured. The loading efficiency of drug was then calculated using the standard curve, resulting in a value of $29.12 \pm 2.71\%$ (Figure 1(g)).

TEM images showed that BT-EV has a cup-shaped morphology (Figure 1(c)). NTA measurements indicated that the hydrodynamic diameter of BT-EV was $139.4 \pm 13.9$ nm (Figure 1(d)). The surface charges of EV and BT-EV were $-19.7 \pm 1.3$ and $-22.6 \pm 2.2$ mV, respectively (Figure 1(e)). The slight changes in diameter and potential may be attributed to the peptide attached to the membrane. These results demonstrate that BT-EV maintains the integrity and properties of EV.

Physiological stability of nanocarriers is of significant importance in the application of drug delivery. To determine the stability of BT-EV under physiological
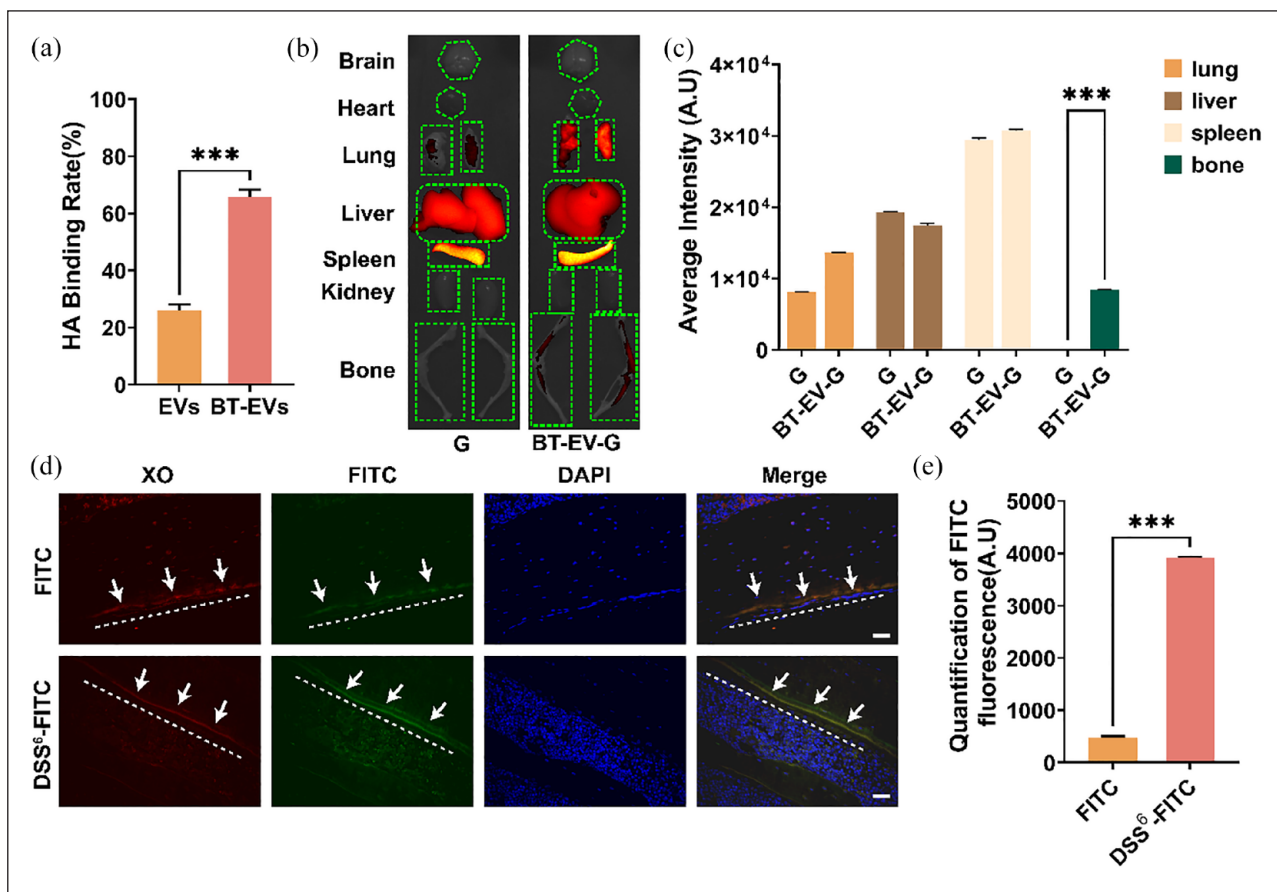
**Figure 2.** Bone-targeting capability in vitro and vivo. (a) In vitro HA binding capacities of EV and BT-EV. (b) Biodistribution of Cy5.5-labelled G or BT-EV-G in mouse. (c) Fluorescence intensity of DiR-labelled G or BT-EV-G in different organs. (d) Fluorescence micrographs from mouse with DSS$^6$-FITC, the red fluorescence represents the bone surfaces labeled xylenol orange (XO), the green fluorescence represents the locally accumulated DSS$^6$-FITC. Scale bar = 50 μm. (e) Fluorescence intensity of FITC or DSS$^6$-FITC. ($n$ = 3; ns, no significant difference; ***$p$ < 0.001).

conditions, we monitored the particle diameter and zeta potential in 50% fetal bovine serum (FBS) for 7 consecutive days by NTA (Figure S2). No obvious changes were observed, indicating that BT-EV had stable physical characteristics.

## Biosafety in vitro and in vivo

To assess the toxicity of BT-EV-G, we investigated whether BT-EV-G therapy caused damage to primary organs such as the heart, liver, spleen, lung, and kidney. After 4 weeks of administration, we carried out H&E staining of the major organs to evaluate the safety of BT-EV-G in vivo. The major organs showed no pathological changes, demonstrating that BT-EV-G had no systemic toxicity (Figure S3). The cytotoxicity of BT-EV-G was evaluated by coculturing it with normal MC3T3-E1 cells at different concentrations. Cell viability was assessed using CCK-8 (Figure S4), and low cytotoxicity was observed.

## Bone-targeting capability in vitro and vivo

The main component of bone is hydroxyapatite (HA), which constitutes 95% of the inorganic part. To evaluate bone affinity in vitro, we compared the HA binding capacity of EVs and BT-EVs. As shown in Figure 2(a), the HA binding rate of BT-EVs (65.92%) was higher than that of EVs (26.01%). This indicates that BT-EVs have a better bone affinity ($p$ < 0.001) than EVs and may enable better delivery of Galunisertib to the bone.

Additionally, we compared the presence of FITC at bone formation surfaces in adult mice injected with FITC-labeled BT and those injected with FITC-labeled BT after pre-injection of xylenol orange, a red fluorescent calcium-binding dye capable of labeling new bone deposition at bone formation surfaces. In Figure 2(d), we observed that bone-formation surfaces, labeled with xylenol orange, were largely co-labeled with BT, labeled with FITC. However, we did not observe co-labeling in the mice injected with FITC-labeled EV.
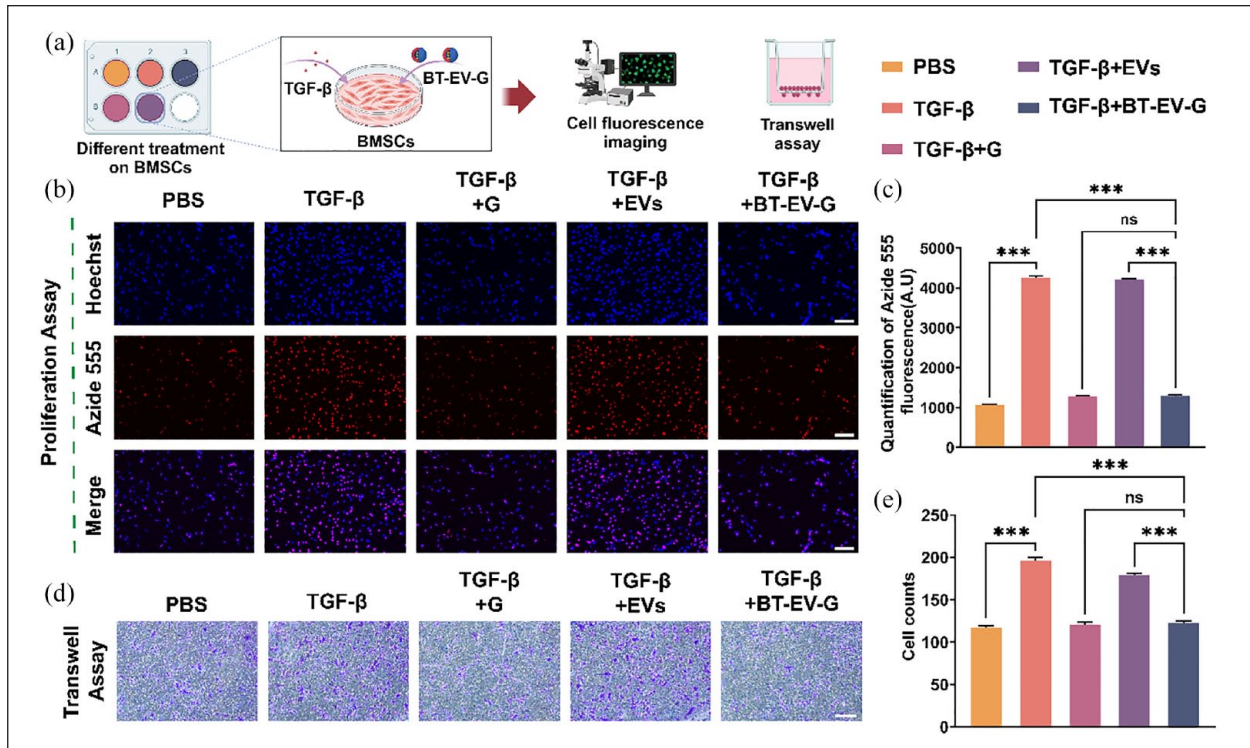
**Figure 3.** BT-EV-G inhibited the Proliferation and Migratoin of BMSCs in vitro. (a) Schematic diagram of experiments. (b) Proliferation Assay of bone marrow mesenchymal stem cells (BMSCs). Hoechst (blue), nuclei; Azide 555(red), newly synthesized DNA. Scale bar = 50 μm. (c) Quantitative analysis of Azide 555. (d) Transwell Assay of bone marrow mesenchymal stem cells (BMSCs). Scale bar = 0.1 mm. (e) Quantitative analysis of the number of crossing cell ($n$ = 3; ns, no significant difference; ***$p$ < 0.001).

Subsequently, we investigated the bone targeting ability of BT-EV-G in vivo. The accumulation of G bone was detected through biophotonic imaging after tail intravenous injection of Cy5.5-labelled G or BT-EV-G into mice. The major organs, including the brain, heart, liver, spleen, lungs, kidneys, bone (tibia and femur), were harvested for imaging. A stronger fluorescent signal was observed in the bones of BT-EV-G-treated mice compared to G-treated mice (Figure 2(b)). The fluorescence signal intensity was recorded for quantitative analysis (Figure 2(c)). The results suggest that BT-EV may enhance bone accumulation of drug.

## BT-EV-G inhibited the differentiation, proliferation, and migration of BMSCs in vitro

In OA, the abnormal TGF-β, when activated, recruits BMSCs and promotes their osteogenic differentiation to form abnormal osteoid islets, which further exacerbates the abnormal stresses in the joints and ultimately promotes the progression of OA.[10] The study investigated the effect of BT-EV-G on BMSCs' migration, proliferation, and differentiation. To mimic the in vivo pathological

environment, we added TGF-β in the experimental groups. Primary BMSCs were successfully cultured (Figure S5). To validate the role of BT-EV-G on BMSCs, PKH26 was used to label BT-EV-G and trace its internalization in BMSCs. Figure S6 shows that PKH26-labelled BT-EV-G (red fluorescence) were efficiently internalized by BMSCs and were evenly distributed around the DAPI-stained nuclei.

The EdU assay indicated that treatment with BT-EV-G inhibited the proliferation of BMSCs (Figure 3(b)). A significant difference was observed between the TGF-β + BT-EV-G group and the TGF-β group($p$ < 0.001), with no difference observed between the TGF-β + BT-EV-G group and the TGF-β + G group (p = ns) (Figure 3(c)). This indicates that the drug-carrying system did not affect the drug release and successfully exerted its influence on BMSC. Furthermore, a Transwell migration assay was conducted to evaluate the migration ability of BMSCs treated with BT-EV-G, as depicted in Figure 3(d). The quantity of migrated BMSCs stimulated by BT-EV-G was significantly lower than that of the other group (Figure 3(e)). In proliferation and migration assays, none of the EVs groups demonstrated significant therapeutic effects.

Subsequently, we observed the effect of BT-EV-G on osteogenic differentiation in vitro through ALP staining and Alizarin Red staining. The deposition of minerals in the extracellular matrix can directly indicate the extent of cell osteogenic differentiation. ALP is a crucial monophosphate hydrolase during cell mineralization and osteogenic differentiation. Since ALP activity is an early indicator of osteogenic differentiation, we detected it through ALP staining in the early differentiation stage. On day 7, BMSCs co-incubated with BT-EV-G exhibited less ALP activity compared to the TGF-β group (Figure 4(b)). After 21 days of osteogenic differentiation induction, the BT-EV-G group showed fewer red mineralization nodules compared to the TGF-β group, as demonstrated in Figure 4(d) using Alizarin Red S, which chelates $Ca^{2+}$ in calcium salt deposition and forms a dark red compound proportional to the degree of extracellular matrix mineralization.

The mRNA expressions of Alkaline phosphatase (ALP), osteogenic-related genes runt-related transcription factor 2 (Runx2), osteocalcin (OCN), osteopontin (OPN), and osterix (OSX) were determined by RT-PCR after incubation with different nanoparticles for 7 days (Figure 4(f)). The representative proteins of osteogenic differentiation, ALP, Runx2, and OCN were detected using immunofluorescent staining (Figure 4(g, i, k)). The overall trend of these results was consistent with the staining results.

The EVs group did not demonstrate a significant impact on osteogenic differentiation or the inhibition thereof. This may be attributed to the utilization of EVs derived from an M0 macrophages source, rather than an M1 or M2 source.

### BT-EV-G attenuates progression of OA in ACLT mice

To examine the impact of BT-EV-G on disease activity and progression in OA, we administered BT-EV-G intravenously to mice after ACLT. The schematic diagram of animal experiments is shown in Figure 5(a). Our results showed that BT-EV-G treatment led to smoother surface cartilage repair and reduced thickness of the calcified cartilage zone (from the tidemark line to the subchondral bone plate) compared to the PBS-treated ACLT controls, as demonstrated by H&E staining, and it is more effective than using G alone (Figure 5(b)). Immunohistochemistry was used to evaluate the levels of osteoarthritis-related proteins in mouse articular cartilage, which can reveal the severity of OA. The expression of MMP-13, aggrecan, and collagen II was normalized by BT-EV-G treatment in ACLT mice compared to PBS-treated ACLT controls, as determined by immunostaining (Figure 5(d, f, h)). To assess the severity of cartilage damage, we applied the OARSI scoring system. The OARSI scores of the BT-EV-G-treated ACLT mice were improved compared to the G-treated ACLT controls (Figure 5(c)). These results

suggested that the therapeutic effect was better when used with drug carriers.

### BT-EV-G amplifies the role of G in supporting subchondral bone association remodeling

The impact of BT-EV-G on the structure of tibial subchondral bone was assessed using micro-CT. Results showed that BT-EV-G significantly decreased the tissue volume (TV) of tibial subchondral bone, reduced trabecular pattern factor (Tb.pf), and increased SBP thickness after ACLT compared to G treatment (Figure 6(a–d)). The number of tartrate-resistant acid phosphatase-positive osteoclast cells and osteoprogenitor Osterix-positive cells consistently increased after ACLT (PBS vs sham). However, this increase in both cell populations was abrogated by BT-EV-G treatment (Figure 6(e, f)).

### BT-EV-G inhibits pSmad2/3-dependent TGF-β signaling pathway in BMSCs

Immunofluorescence staining of Nestin revealed that BT-EV-G significantly reduced the increase in the number of MSCs in the subchondral bone post ACLT compared to PBS treatment (Figure 7(a)). As high levels of active TGF-β recruit MSCs in the subchondral bone marrow, we investigated whether BT-EV-G could directly inhibit TGF-β signaling in MSCs. The inhibition of TGF-β signaling in subchondral bone cells by BT-EV-G was further validated by immunohistochemistry staining of pSmad2/3 (Figure 7(c)). Specifically, the number of pSmad2/3-positive cells in the subchondral bone of ACLT mice treated with PBS was significantly increased, but this effect was attenuated with BT-EV-G to levels comparable with those of sham mice.

## Conclusions

The results of this study indicate that engineered EVs carrying small molecule drugs to in vivo mouse OA joints have the potential to inhibit aberrant ossification and delay the pathological progression of OA. This highlights the promising prospects of subchondral bone as a therapeutic target for OA and EVs as a drug carrier, advancing the translation of theoretical research to clinical applications.

A multitude of studies have investigated how to counteract the deleterious effects of TGF-β in the subchondral bone microenvironment in OA. Cui et al.[55] applied HF (a traditional Chinese medicine extract) by intraperitoneal administration in OA mice to attenuate osteoarthritis by inhibiting TGF-β activity and H-type angiogenesis in the subchondral bone. Zhen et al.[56] utilized a TGF-β inhibitor (SB-505124) by intraperitoneal injection to inhibit TGF-β signaling in mesenchymal stem cells of subchondral bone,
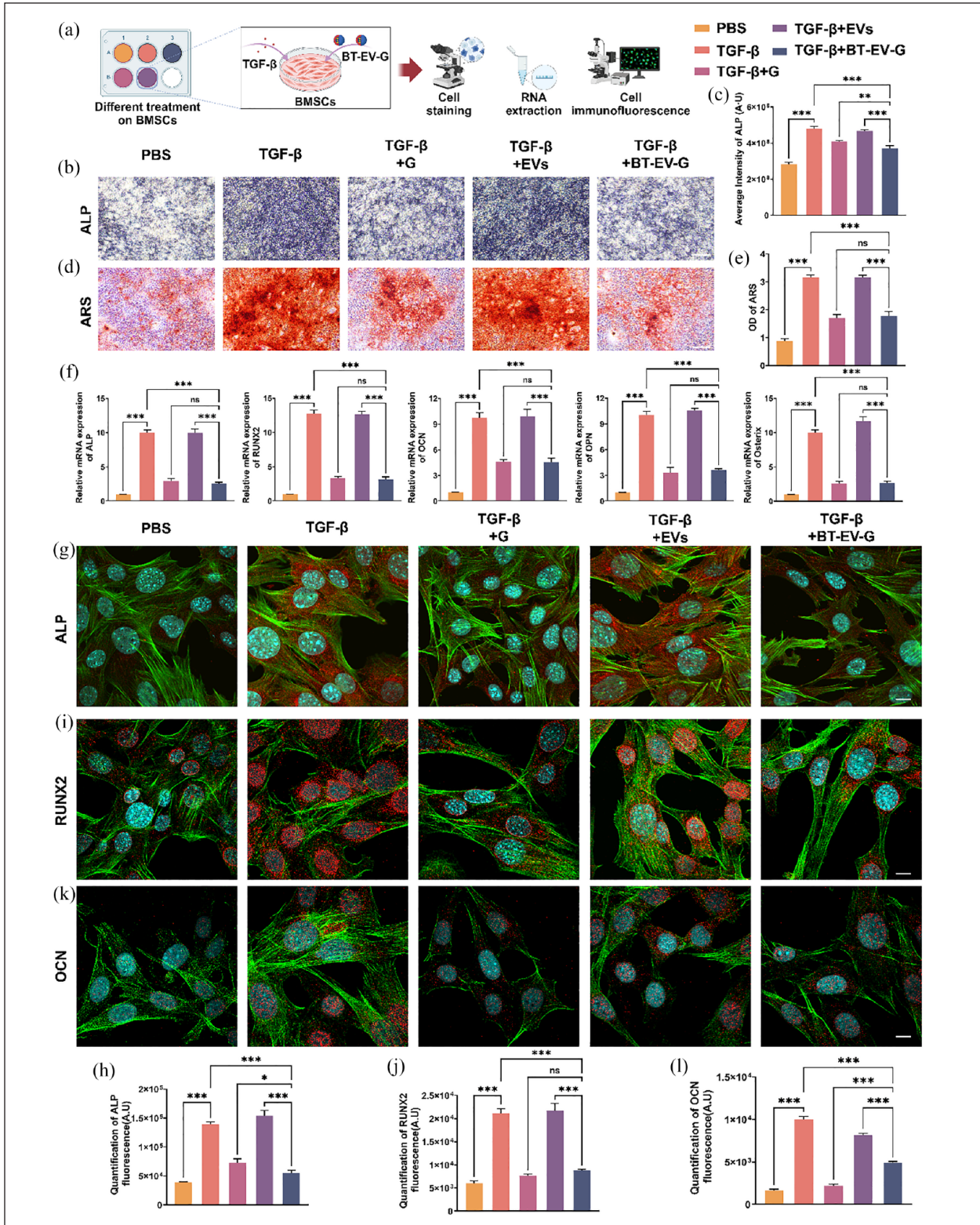
**Figure 4.** BT-EV-G inhibited the Differentiation of BMSCs in vitro. (a) Schematic diagram of experiments. (b) Alkaline phosphatase (ALP) staining of mouse bone marrow mesenchymal stem cells (BMSCs). Scale bar = 0.1 mm. (c) Quantitative analysis of ALP staining. (d) Osteogenic differentiation of BMSCs observed by Alizarin Red staining. Scale bar = 0.1 mm. (e) Quantitative analysis of ARS staining. (f) Relative mRNA expression of osteogenesis-related genes (ALP, Runx2, OCN, OPN and Osterix) after incubation with different nano-particles for 7 days. (g, i, k) Representative immunofluorescence images showing expression of osteogenic differentiation-related proteins (ALP, Runx2 and OCN) by BMSCs after different treatments for 3 days. Scale bar = 10 μm. (h, j, l) Quantitative analysis of fluorescence intensity of OCN, Runx2 and ALP. ($n$ = 3; ns, no significant difference; *$p$ < 0.05. ***$p$ < 0.001).
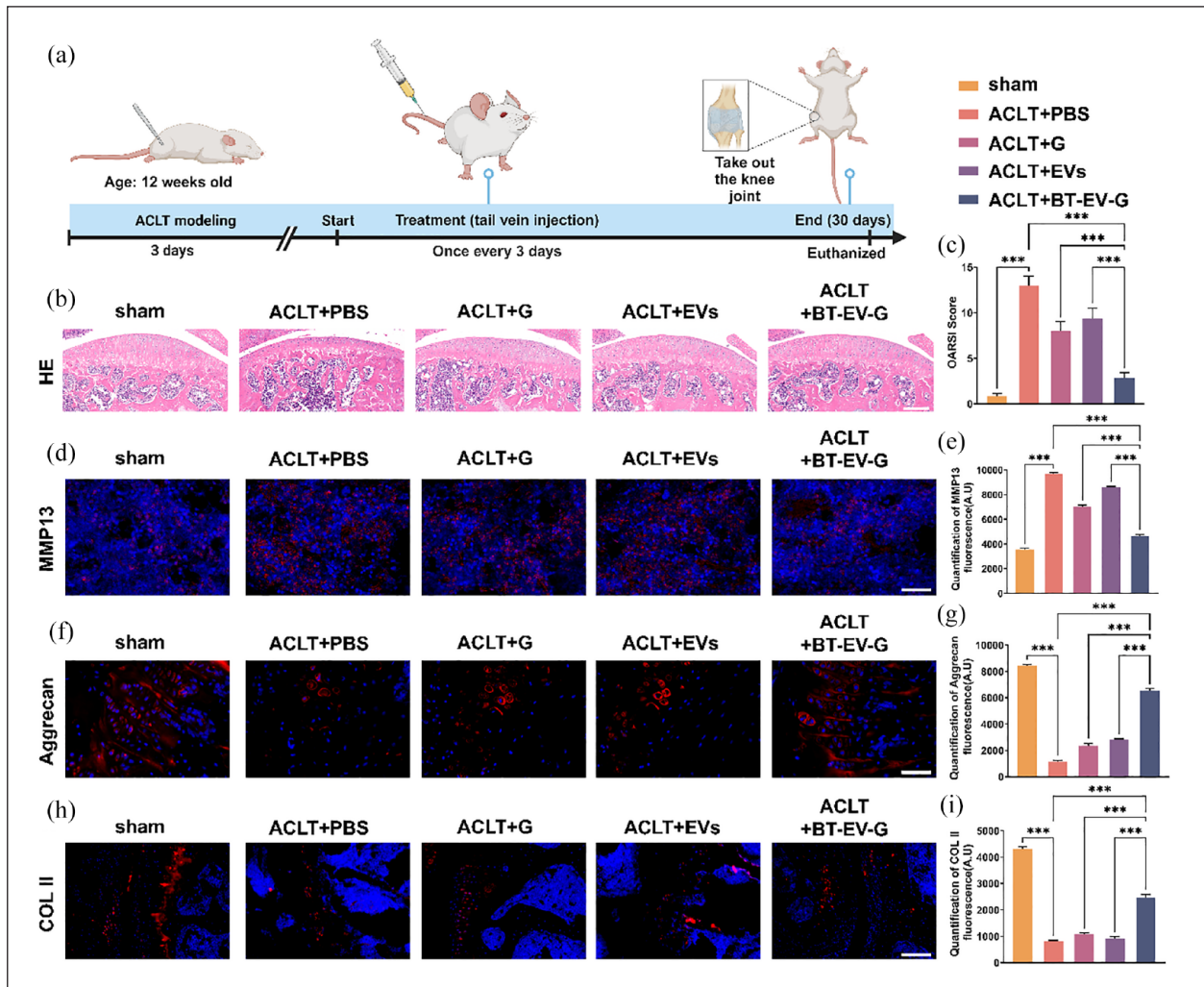
**Figure 5.** BT-EV-G attenuates progression of OA in ACLT mice. (a) Schematic diagram of animal experiments. (b) H&E staining of the medial compartments of the knee joints. Scale bar = 500 μm. (c) OASRT score for assessing the cartilage degradation. (d, f, h) Immunostaining of MMP13, aggrecan, and COL II in articular cartilage at 30 days post operation. Scale bar = 50 μm. (e, g, i) Quantitative analysis of MMP13, aggrecan and COL II. ($n$ = 3; ns, no significant difference; ***$p$ < 0.001).

thereby reducing osteoarthritis. Zhong et al.[57] injected Nangibotide intraperitoneally to reduce osteoarthritis by inhibiting osteoblast apoptosis and TGF-β activity in subchondral bone. Although intraperitoneal injections are relatively simple to administer and highly absorbable. However, the injection dose is large, and there is irritation. Furthermore, it is difficult to ensure that an effective drug concentration is achieved locally in the joint. This method is only applicable to animal experiments, and it is difficult to carry out clinical translation. Consequently, the development of a novel drug delivery method is imperative.

The use of EVs as emerging drug carriers has gained increasing attention, with a growing number of studies demonstrating their efficacy in oncology and cardiovascular fields.[58] Building upon this premise, we took macrophage-derived EVs as a blueprint and modified the EVs membrane with targeted peptides to construct a drug delivery system with low immunogenicity, low clearance, and high targeting. In validation experiments, BT-EV-G demonstrated good biosafety and subchondral bone targeting. The results demonstrated that BT-EV-G inhibited TGF-β activity and blocked the proliferation, migration, and osteogenic differentiation of BMSCs in both in vivo and in vitro experiments. Furthermore, BT-EV-G successfully delayed the pathologic progression of subchondral bone in OA mice in vivo. In comparison to the aforementioned experiments, the amount of drug used was reduced from the milligram level to the microgram level, and the active targeting of subchondral bone was increased. This approach facilitates the translation of TGF-β inhibitor findings from cellular and
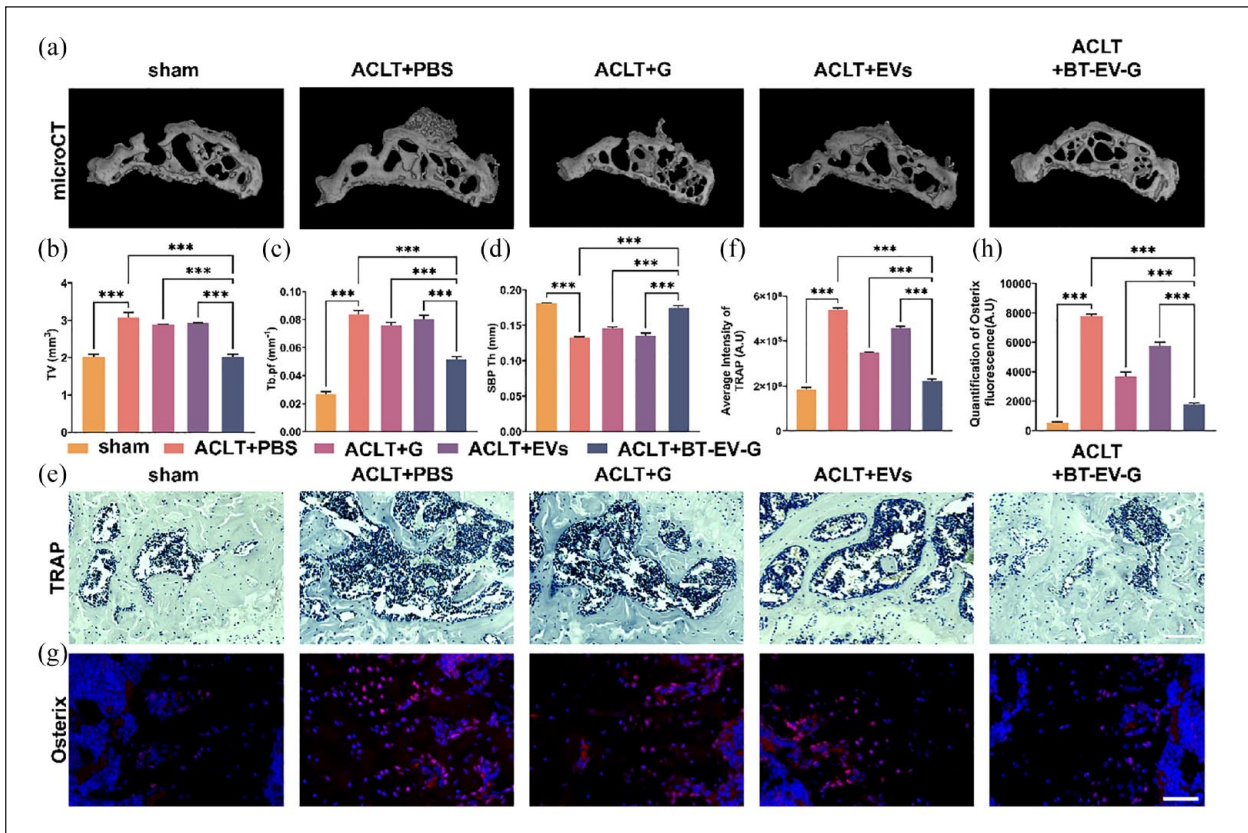
**Figure 6.** BT-EV-G amplifies the role of G in supporting subchondral bone association remodeling. (a) Representative three-dimensional micro-CT images of sagittal views of subchondral bone medial compartment at 30 days after sham operation or ACLT surgery. (b–d) Quantitative micro-CT analysis of tibial subchondral bone of total tissue volume (TV), trabecular pattern factor (Tb. pf) and subchondral bone plate thickness (SBP). (e) Tartrate-resistant acid phosphatase (TRAP) staining at 30 days after surgery. Scale bar = 50 μm. (f) Quantitative anlysis of intensity of TRAP. (g) Immunohistochemical staining of Osterix-positive cells (red) in subchondral bone 30 days after surgery. Scale bar = 50 μm. (h) Quantiative analysis of intensity of Osterix. ($n = 3$; ns, no significant difference; ***$p < 0.001$).

animal experiments to the clinical setting, providing a more realistic representation of the real-world application of these inhibitors in the context of OA subchondral bone.

This study also has some limitations. One area that requires further investigation is the drug release behavior of EVs in the subchondral bone microenvironment. This should be elucidated in future studies. The subchondral bone microenvironment is a hypoxic and acidic environment, which presents a challenge for drug release in

specific environments.[59] Another area that requires further study is the accidental accumulation of EVs in non-target organs (liver, lung, etc.).

In conclusion, we developed a promising tool for targeted delivery of TGF-β inhibitors to block the activation of abnormal ossification. We validated the therapeutic efficacy of this system in early OA, which showed good targeting in subchondral bone. Further exploration of the use of this approach for other bone disorders is warranted.
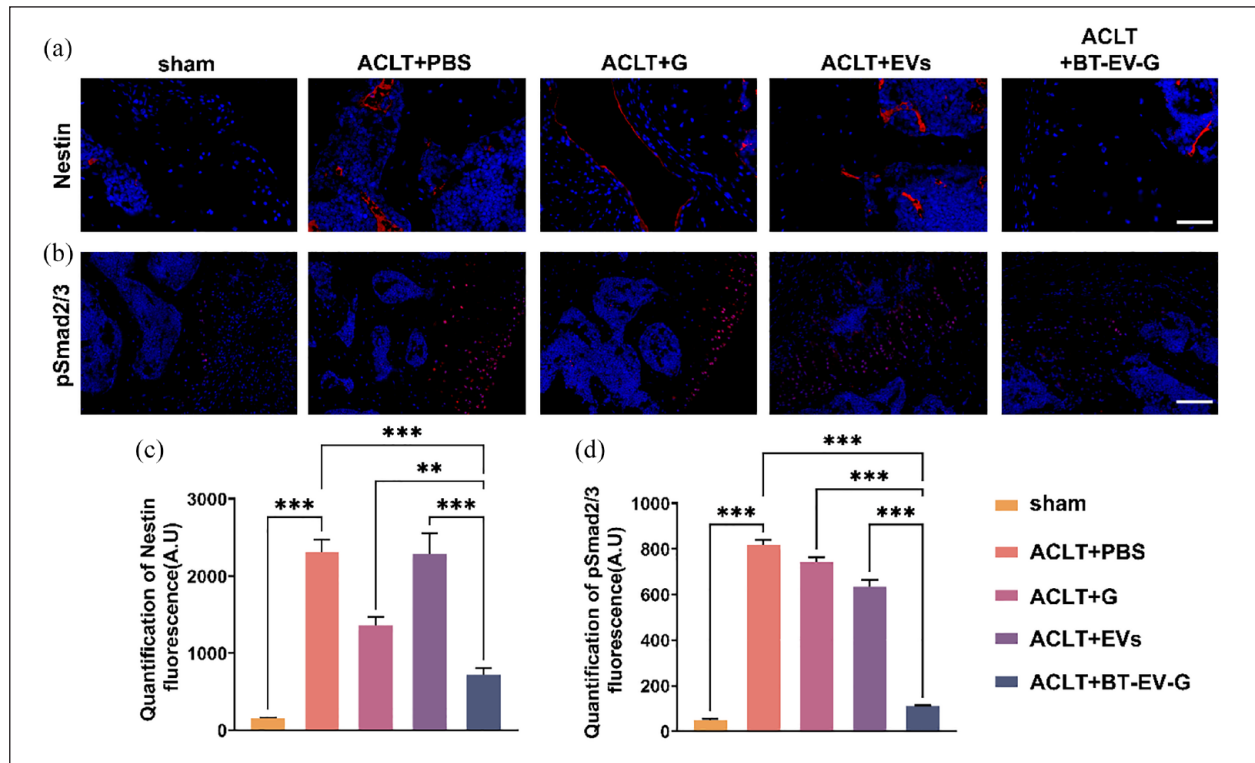
**Figure 7.** BT-EV-G inhibits pSmad2/3-dependent TGF-β signaling pathway in BMSCs. (a) Immunofluorescence staining for Nestin in sagittal sections of subchondral bone medial compartment 30 days post-surgery. Scale bar = 100 μm. (b) Quantitative analysis of Nestin staining. (c) Immunofluorescence staining of pSmad2/3-positive cells in sagittal sections of subchondral bone medial compartment 30 days post-surgery. Scale bar = 100 μm. (d) Quantitative analysis of pSmad2/3 staining. ($n$ = 3; ns, no significant difference; **$p$ < 0.01. ***$p$ < 0.001).

## Data availability statement

All relevant data are included in the paper and/or its supplementary information files.

## Declaration of conflicting interests

The author(s) declared no potential conflicts of interest with respect to the research, authorship, and/or publication of this article.

## ORCID iDs

Zhaopu Jing (iD) https://orcid.org/0000-0002-6027-2759
Xiaoqian Dang (iD) https://orcid.org/0009-0004-0274-6794

## Supplemental material

Supplemental material for this article is available online.

## References

1. Martel-Pelletier J, Barr AJ, Cicuttini FM, et al. Osteoarthritis. *Nat Rev Dis Primers* 2016; 2: 16072.
2. Global Burden of Disease Study 2013 Collaborators. Global, regional, and national incidence, prevalence, and years lived with disability for 301 acute and chronic diseases and injuries in 188 countries, 1990-2013: a systematic analysis for the Global Burden of Disease Study 2013. *Lancet* 2015; 386: 743–800.
3. Hiligsmann M, Cooper C, Arden N, et al. Health economics in the field of osteoarthritis: an expert's consensus paper from the European Society for Clinical and Economic Aspects of Osteoporosis and Osteoarthritis (ESCEO). *Semin Arthritis Rheum* 2013; 43: 303–313.
4. Bannuru RR, Osani MC, Vaysbrot EE, et al. OARSI guidelines for the non-surgical management of knee, hip, and polyarticular osteoarthritis. *Osteoarthritis Cartilage* 2019; 27: 1578–1589.
5. Sharma L. Osteoarthritis of the knee. *N Engl J Med* 2021; 384: 51–59.
6. Oo WM, Little C, Duong V, et al. The development of disease-modifying therapies for osteoarthritis (DMOADs): the evidence to date. *Drug Des Devel Ther* 2021; 15: 2921–2945.

7. Felson DT. Identifying different osteoarthritis phenotypes through epidemiology. *Osteoarthritis Cartilage* 2010; 18: 601–604.

8. Bierma-Zeinstra SMA and Verhagen AP. Osteoarthritis subpopulations and implications for clinical trial design. *Arthritis Res Ther* 2011; 13: 213.

9. Oo WM and Hunter DJ. Disease modification in osteoarthritis: are we there yet? *Clin Exp Rheumatol* 2019; 37 Suppl 120: 135–140.

10. Hu W, Chen Y, Dou C, et al. Microenvironment in subchondral bone: predominant regulator for the treatment of osteoarthritis. *Ann Rheum Dis* 2021; 80: 413–422. **[AQ: 3]**

11. Żylińska B, Sobczyńska-Rak A, Lisiecka U, et al. Structure and pathologies of articular cartilage. *In Vivo* 2021; 35: 1355–1363.

12. Bruno MC, Cristiano MC, Celia C, et al. Injectable drug delivery systems for osteoarthritis and rheumatoid arthritis. *ACS Nano* 2022; 16: 19665–19690.

13. Khalid A, Persano S, Shen H, et al. Strategies for improving drug delivery: nanocarriers and microenvironmental priming. *Expert Opin Drug Deliv* 2017; 14: 865–877.

14. Younis MA, Tawfeek HM, Abdellatif AAH, et al. Clinical translation of nanomedicines: Challenges, opportunities, and keys. *Adv Drug Deliv Rev* 2022; 181: 114083.

15. Herrmann IK, Wood MJA and Fuhrmann G. Extracellular vesicles as a next-generation drug delivery platform. *Nat Nanotechnol* 2021; 16: 748–759.

16. Hussain S, Vanoirbeek JAJ and Hoet PHM. Interactions of nanomaterials with the immune system. *Wiley Interdiscip Rev Nanomed Nanobiotechnol* 2012; 4: 169–183.

17. Gudbergsson JM, Jønsson K, Simonsen JB, et al. Systematic review of targeted extracellular vesicles for drug delivery – considerations on methodological and biological heterogeneity. *J Control Release* 2019; 306: 108–120.

18. Elsharkasy OM, Nordin JZ, Hagey DW, et al. Extracellular vesicles as drug delivery systems: why and how? *Adv Drug Deliv Rev* 2020; 159: 332–343.

19. Guo M, Wu F, Hu G, et al. Autologous tumor cell-derived microparticle-based targeted chemotherapy in lung cancer patients with malignant pleural effusion. *Sci Transl Med* 2019; 11: eaat5690.

20. Gao X, Ran N, Dong X, et al. Anchor peptide captures, targets, and loads exosomes of diverse origins for diagnostics and therapy. *Sci Transl Med* 2018; 10: eaat0195.

21. Alvarez-Erviti L, Seow Y, Yin H, et al. Delivery of siRNA to the mouse brain by systemic injection of targeted exosomes. *Nat Biotechnol* 2011; 29: 341–345.

22. Ridder K, Keller S, Dams M, et al. Extracellular vesicle-mediated transfer of genetic information between the hematopoietic system and the brain in response to inflammation. *PLoS Biol* 2014; 12: e1001874.

23. van Dongen HM, Masoumi N, Witwer KW, et al. Extracellular vesicles exploit viral entry routes for cargo delivery. *Microbiol Mol Biol Rev* 2016; 80: 369–386.

24. Heusermann W, Hean J, Trojer D, et al. Exosomes surf on filopodia to enter cells at endocytic hot spots, traffic within endosomes, and are targeted to the ER. *J Cell Biol* 2016; 213: 173–184.

25. Millard M, Yakavets I, Piffoux M, et al. mTHPC-loaded extracellular vesicles outperform liposomal and free mTHPC formulations by an increased stability, drug delivery efficiency and cytotoxic effect in tridimensional model of tumors. *Drug Deliv* 2018; 25: 1790–1801.

26. Lai CP, Mardini O, Ericsson M, et al. Dynamic biodistribution of extracellular vesicles in vivo using a multimodal imaging reporter. *ACS Nano* 2014; 8: 483–494.

27. Wiklander OPB, Nordin JZ, O'Loughlin A, et al. Extracellular vesicle in vivo biodistribution is determined by cell source, route of administration and targeting. *Journal of Extracellular Vesicles* 2015; 4: 26316. DOI: 10.3402/jev. v4.26316.

28. Yong T, Wang D, Li X, et al. Extracellular vesicles for tumor targeting delivery based on five features principle. *J Control Release* 2020; 322: 555–565.

29. Tran PHL, Xiang D, Tran TTD, et al. Exosomes and nano-engineering: a match made for precision therapeutics. *Adv Mater* 2020; 32: e1904040.

30. Jia G, Han Y, An Y, et al. NRP-1 targeted and cargo-loaded exosomes facilitate simultaneous imaging and therapy of glioma in vitro and in vivo. *Biomaterials* 2018; 178: 302–316.

31. Wang Y, Chen X, Tian B, et al. Nucleolin-targeted extracellular vesicles as a versatile platform for biologics delivery to breast cancer. *Theranostics* 2017; 7: 1360–1372.

32. Lin Q, Qu M, Zhou B, et al. Exosome-like nanoplatform modified with targeting ligand improves anti-cancer and anti-inflammation effects of imperialine. *J Control Release* 2019; 311–312: 104–116.

33. Liang Y, Xu X, Li X, et al. Chondrocyte-targeted MicroRNA delivery by engineered exosomes toward a cell-free osteoarthritis therapy. *ACS Appl Mater Interfaces* 2020; 12: 36938–36947.

34. Hunter DJ and Bierma-Zeinstra S. Osteoarthritis. *Lancet* 2019; 393: 1745–1759.

35. He C, Zheng S, Luo Y, et al. Exosome theranostics: biology and translational medicine. *Theranostics* 2018; 8: 237–255.

36. Dang XTT, Kavishka JM, Zhang DX, et al. Extracellular vesicles as an efficient and versatile system for drug delivery. *Cells* 2020; 9: 2191.

37. Chen Y, Wu X, Li J, et al. Bone-targeted nanoparticle drug delivery system: an emerging strategy for bone-related disease. *Front Pharmacol* 2022; 13: 909408.

38. Zhang G, Guo B, Wu H, et al. A delivery system targeting bone formation surfaces to facilitate RNAi-based anabolic therapy. *Nat Med* 2012; 18: 307–314.

39. Das CK, Jena BC, Banerjee I, et al. Exosome as a novel shuttle for delivery of therapeutics across biological barriers. *Mol Pharm* 2019; 16: 24–40.

40. Fan J, Lee C-S, Kim S, et al. Generation of small RNA-modulated exosome mimetics for bone regeneration. *ACS Nano* 2020; 14: 11973–11984.

41. Zhang S, Chu WC, Lai RC, et al. Exosomes derived from human embryonic mesenchymal stem cells promote osteochondral regeneration. *Osteoarthritis Cartilage* 2016; 24: 2135–2140.

42. Jiang S, Tian G, Yang Z, et al. Enhancement of acellular cartilage matrix scaffold by Wharton's jelly mesenchymal stem cell-derived exosomes to promote osteochondral regeneration. *Bioact Mater* 2021; 6: 2711–2728.

43. Salunkhe S, Dheeraj Basak M, et al. Surface functionalization of exosomes for target-specific delivery and in vivo imaging & tracking: Strategies and significance. *J Control Release* 2020; 326: 599–614.

44. Kimiz-Gebologlu I and Oncel SS. Exosomes: Large-scale production, isolation, drug loading efficiency, and biodistribution and uptake. *J Control Release* 2022; 347: 533–543.

45. Zhang S, Xie F, Li K, et al. Gold nanoparticle-directed autophagy intervention for antitumor immunotherapy via inhibiting tumor-associated macrophage M2 polarization. *Acta Pharm Sin B* 2022; 12: 3124–3138.

46. Mathieu M, Martin-Jaular L, Lavieu G, et al. Specificities of secretion and uptake of exosomes and other extracellular vesicles for cell-to-cell communication. *Nat Cell Biol* 2019; 21: 9–17.

47. Zhou X, Cornel EJ, Fan Z, et al. Bone-targeting polymer vesicles for effective therapy of osteoporosis. *Nano Lett* 2021; 21: 7998–8007.

48. Stuart AJ and Smith DA. Use of the fluorochromes xylenol orange, calcein green, and tetracycline to document bone deposition and remodeling in healing fractures in chickens. *Avian Dis* 1992; 36: 447–449.

49. Gronthos S, Zannettino AC, Graves SE, et al. Differential cell surface expression of the STRO-1 and alkaline phosphatase antigens on discrete developmental stages in primary cultures of human bone cells. *J Bone Miner Res* 1999; 14: 47–56.

50. Gao J, Sun J, Li H, et al. Lyophilized HER2-specific PEGylated immunoliposomes for active siRNA gene silencing. *Biomaterials* 2010; 31: 2655–2664.

51. Zhai M, Zhu Y, Yang M, et al. Human mesenchymal stem cell derived exosomes enhance cell-free bone regeneration by altering their miRNAs profiles. *Adv Sci* 2020; 7: 2001334.

52. Zhu J, Liu B, Wang Z, et al. Exosomes from nicotine-stimulated macrophages accelerate atherosclerosis through miR-21-3p/PTEN-mediated VSMC migration and proliferation. *Theranostics* 2019; 9: 6901–6919.

53. Cui Y, Guo Y, Kong L, et al. A bone-targeted engineered exosome platform delivering siRNA to treat osteoporosis. *Bioact Mater* 2022; 10: 207–221.

54. Pritzker KPH, Gay S, Jimenez SA, et al. Osteoarthritis cartilage histopathology: grading and staging. *Osteoarthritis Cartilage* 2006; 14: 13–29.

55. Cui Z, Crane J, Xie H, et al. Halofuginone attenuates osteoarthritis by inhibition of TGF-β activity and H-type vessel formation in subchondral bone. *Ann Rheum Dis* 2016; 75: 1714–1721.

56. Zhen G, Wen C, Jia X, et al. Inhibition of TGF-β signaling in mesenchymal stem cells of subchondral bone attenuates osteoarthritis. *Nat Med* 2013; 19: 704–712.

57. Zhong Y, Xu Y, Xue S, et al. Nangibotide attenuates osteoarthritis by inhibiting osteoblast apoptosis and TGF-β activity in subchondral bone. *Inflammopharmacology* 2022; 30: 1107–1117.

58. Escudé Martinez de Castilla P, Tong L, Huang C, et al. Extracellular vesicles as a drug delivery system: a systematic review of preclinical studies. *Adv Drug Deliv Rev* 2021; 175: 113801.

59. Hu Y, Chen X, Wang S, et al. Subchondral bone microenvironment in osteoarthritis and pain. *Bone Research* 2021; 9: 20.s